SRYAHWA PUBLICATIONS

Annals of Ecology and Environmental Science
ISSN: 2637-5338 | Volume 8, Issue 1, 2026
https://doi.org/10.22259/2637-5338.0801001

RESEARCH ARTICLE

Spatiotemporal Windblown Sand Patterns in the Bon Lanuar Region (Mauritania): Insights from InSAR Coherence and K-means Clustering

Yaghoub Ahmed Deya, Mohamed Henoune, Dah Ould Ahmedou

Department of Mathematics and Computer Science, Faculty of Science and Technology, Mauritania.

Received: 04 February 2026 Accepted: 17 February 2026 Published: 24 February 2026

Corresponding Author: Yaghoub Ahmed Deya, Department of Mathematics and Computer Science, Faculty of Science and Technology, Street, Nouakchott State, Mauritania.

Abstract

Wind erosion and sand accumulation in the Bon Lanuar region of northwest Mauritania pose significant threats to infrastructure, including railways, high- ways, housing, and solar farms. Understanding the dynamics of wind and sand in this region is crucial for promoting sustainable development in similar arid areas worldwide. This study analyzes 31 Sentinel-1 interferometric coherence images acquired between March and December 2020. We applied an unsupervised k- means clustering algorithm to these images and their coherence ratios to map spatiotemporal changes in eolian sand accumulation patterns. Three areas par- ticularly affected by sand activity were identified: a field of barchan dunes west of Bon Lanuar, the city itself, and the railway and highway lines crossing it. The k-means classification revealed that 19.4% of the dunes in the barchan field exhibit high activity levels, with an annual erosion rate of 3.84% in the northern and western directions. Additionally, 15.56% sedimentation was observed along transport routes and near urban areas. Coherence ratio analysis indicated higher levels of sand activity during spring and summer, driven by prevailing northeast winds, compared to autumn and winter.

Keywords: Aeolian Processes, InSAR Coherence, Spatiotemporal Monitoring, K-Means Classification, Nasa Meteorological Data.

1. Introduction

The study of windblown dunes, characteristic of desert environments, has prompted interdisciplinary research combining theoretical, numerical, and experimen- tal approaches. Bagnold (1941) laid the foundations for sediment transport by wind by identifying a threshold friction velocity for grain entrainment [6]. Tsoar and Pye (1987) [81] further explored the dynamic mechanisms of morphological evolution and dune migration, highlighting different types of dunes (barchans, linear dunes, dome dunes, etc.) and their strong sensitivity to prevailing wind conditions. More recently, Zeeshan Ali et al. (2019) [3] conducted a review on saltation in turbulent wall flows, while Kok et al. (2012) [47] explored the overall physics of wind-driven sand and dust transport. Numerical models, such as those developed by Zhang et al. (2021) [86] and Jiang et al. (2014) [40], have simulated dune movements. Concurrently, experimen- tal studies such as that of Lu¨ et al. (2021) [36] validated theories in wind tunnels, and Yao et al. (2007) [83] examined the migration of real dunes in the Alxa Desert using in situ and satellite data. While these in situ studies remain essential for finely characterizing aeolian processes at the local scale, advanced satellite remote sensing techniques have recently expanded the analytical perspectives on dune dynamics to much broader spatial and temporal scales.

Remote sensing techniques, particularly Synthetic Aperture Radar (SAR) inter- ferometry (InSAR)

Citation: Yaghoub Ahmed Deya, Mohamed Henoune, Dah Ould Ahmedou. Spatiotemporal Windblown Sand Patterns in the Bon Lanuar Region (Mauritania): Insights from InSAR Coherence and K-means Clustering. Annals of Ecology and Environmental Science. 2026; 8(1): 01-17.

(Hanssen, 2001 [29]; Rosen et al., 2000 [69]; Bamler and Hartl,1998 [7]; Small, 1998 [76]; Massonnet and Rabaute, 1993 [57]; Madsen et al., 1993 [55]), have proven essential for studying dune movements at large scales.

The analysis of the temporal decorrelation of InSAR signals through the coherence ratio provides a key indicator of the geomorphological changes experienced by dunes (Lee and Liu, 2001 [32]; Schepanski et al., 2012 [72]). Numerous studies have employed InSAR to explore various phenomena, ranging from sedimentation (Abba et al., 2019 [1]) to dune dynamics (Havivi et al., 2018 [30]; Li et al., 2019) and sudden flood detection (Schepanski et al., 2012 [72]). The use of interferometric coherence enables the map- ping of dune field activity and desertification processes (Yague-Martinez et al., 2016; Grandin, 2016; Bodart and Ozer, 2007 [8]). Multi-temporal analyses also open oppor- tunities for studying the spatiotemporal evolution of these phenomena (Manzoni et al., 2021 [56]; Hugenholtz et al., 2012 [38]).

In this context, the Sentinel-1 radar data from the European Space Agency (ESA), launched in 2014 as part of the Copernicus program (ESA, 2018, 2019), are particu- larly suited for this research. This C-band radar mission, comprising Sentinel-1A and Sentinel-1B, allows for detailed high-resolution spatiotemporal interferometric analy- ses, as demonstrated by Kim et al. (2020, 2021) [43, 44] in Mongolia. Other studies, such as those by Abdelkareem et al. (2020) [2], and Havivi et al. (2018) [30], have also highlighted the potential of Sentinel-1 for monitoring desert dune activity.

However, few studies have focused on wind dynamics in Boulenouar, a region sub- ject to intense wind activity, according to meteorological data from the NASA POWER platform. Sand encroachment threatens socio-economic infrastructures, with barchan dunes capable of migrating up to 23 meters per year (Hachemi et al., 2013 [28]; Ozer et al., 2017). This work aims to address this methodological gap by combining InSAR, the coherence ratio, and K-means classification to monitor wind dynamics in the Boulenouar region, while developing a semi-automatic procedure to map eroded/sedimented areas.

K-means algorithms, although simple and widely used for data exploration and pattern recognition (Dhanachandra et al., 2015 [14]; Nagpal et al., 2013 [59]; Jain, 2010 [39]), pose the challenge of determining the optimal number of clusters. In our study, we adopted the silhouette score (Rousseeuw, 1987) [68] to define this parameter, thus facilitating the analysis and segmentation of SAR images essential for understanding geomorphological dynamics in desert environments (Li and Chen, 2007 [49]; Liu et al., 2019 [52]; Duan et al., 2018 [15]).

Following a literature review, Section 2 will present the Sentinel-1 data from 2020-2021 on Boulenouar and the methods employed, followed by the results and their interpretations in Section 3. Section 4 will relate these results to aeolian pro- cesses and the meteorological data from NASA POWER (https://power.larc.nasa.gov/ data-access-viewer/), while discussing the risks of sand encroachment and potential pathways for sustainable land management.

2. Materials and Methods

2.1 Study Area

The study area is Boulenouar, located in the Nouadhibou region of Mauritania, at coordinates 21.17 N - 16.31 W, near the railway (Figure 1). The climate is desert-like, with temperatures ranging from 25 C to 45 C and annual precipitation of approx- imately 10 mm (World Bank, 2021) [82]. Northeasterly winds drive the migration of sand dunes that can reach up to 23 meters per year (Hachemi et al., 2013 [28]), degrading infrastructure such as roads and railways. The region features barchan and transverse dunes, with initiatives aimed at preserving biodiversity and supporting local livelihoods (UNDP, 2014) [63].

2.2 Sentinel-1B Data

Temporal coherences were generated from 31 SAR images of Sentinel-1B operating in C-band, acquired between February 2020 and February 2021, with a temporal resolu- tion of 12 days, sourced from ASF data (https://search.asf.alaska.edu/). The images, collected in Interferometric Wide (IW) mode with VV/VH polarization and a spatial resolution of 5x20 m (SLC data), provided complete coverage of the study area on a descending orbit, track 23. This temporal resolution facilitated frequent mapping and isolation of wind-induced morphological changes while minimizing the effects of vegeta- tion and precipitation. This high-resolution SAR dataset enabled an in-depth analysis of dynamic surface processes influenced by climatic conditions during the study year. We calculate coherence ratios to highlight areas of decorrelation. While coherence losses are already visible in the interferograms, this method quantifies the differences between two interferograms covering distinct time periods. In our case, we compared two interferograms: one during a period of strong wind activity (high winds and no precipitation) and the other during a period with significant rainfall recorded between the acquisitions.

The study area, Boulenouar (Mauritania), is characterized by a hyper-arid desert climate with an average annual precipitation of only 10 mm (World Bank, 2021) [82]. These rare and irregular precipitation events are insufficient to induce significant changes in soil properties or to support sustainable vegetation cover. Although the region may show limited seasonal vegetation growth, no significant cover was observed for the period analyzed by the interferograms. This aligns with the findings of Schmidt and Karnieli (2000) [73], who demonstrated that vegetation growth in arid and semi-arid regions responds to precipitation with a temporal lag of 1 to 2 months, depending on the phenotype. Furthermore, as shown by Hugenholtz et al. (2012) [38], arid environments with low biomass typically generate minimal signals in interferometric analyses.

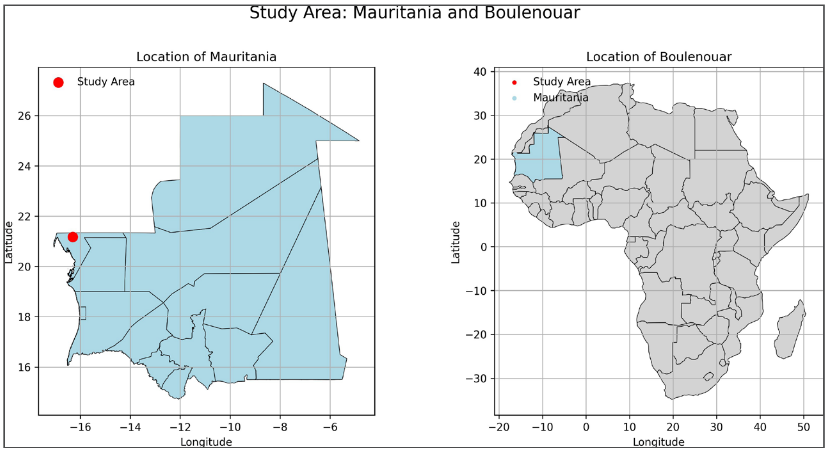

Figure 1. *Map of the Boulenouar study area in Mauritania, showing its geographical location around 21.17 N - 16.31 W.*

The temporal resolution of the interferograms (12 days) used in this study facilitates frequent mapping of wind-induced morphological changes, while minimizing the effects of vegetation and precipitation. Pairs of interferometric data with short temporal intervals, like those analyzed here, are less affected by the impacts of vegetation growth compared to longer periods (e.g., 70 days), where decorrelation due to vegetation is more likely (Schmidt and Karnieli, 2000 [73]).

Stationary decorrelations, such as those due to viewing geometry or topographic effects, are eliminated in ratio images, allowing the emergence of differences in decorrelation caused by other factors. As demonstrated by Lee and Liu (2001) [32], this approach helps separate geometric effects from changes related to environmental or climatic phenomena. In this context, the low coherence during intense wind periods may reflect a dominant contribution from wind processes, with negligible influence from vegetation.

The coherence ratio method can only be applied to interferometric pairs with small spatial baseline differences. Indeed, as noted by Ferretti et al. (2007) [20], large variations in viewing geometry between two interferograms could introduce biases in the comparison, invalidating the assumption of geometric similarity. Havivi et al. (2018) [30] also demonstrated that using short baseline data significantly improves accuracy in monitoring mobile dunes.

The analysis shows that variations in coherence are primarily linked to aeolian processes, which dominate in this region of low precipitation and limited vegetation cover. These results confirm the utility of coherence ratios for analyzing dune dynamics in desert environments.

2.3 Climatic Data

Daily meteorological data from NASA’s MERRA-2 model reanalyses were examined to identify windy and rainy events likely to cause erosion and sediment leaching. These data, accessible via the CERES portal (https://power.larc.nasa.gov/data-access-viewer/), include estimates of maximum wind speed at 10 m (WS10M MAX, in ms) and total precipitation (PRECTOTCORR, in mmday) for the period from February 8, 2020, to February 26, 2021, at the location 21.17 N, -16.31 W, with an average altitude of 53.38 m. Although there are no in-situ measurements, these reanalyses provide the best estimates of wind and precipitation parameters for this coastal region. A detailed analysis of these meteorological data should enhance the understanding of local sediment dynamics and its evolution in relation to climatic conditions.

2.4 Methodology

This study employed a multi-step approach to analyze spatiotemporal patterns of wind-driven sand accumulation in Boulenouar, Mauritania (Figure 3). The key steps include.

2.4.1 InSAR Processing

The process began with the acquisition of Sentinel-1 data spanning from February 2020 to February 2021, obtained from ASF data archives (https://search.asf.alaska.edu/). These datasets were then subjected to Interferometric Synthetic Aperture Radar (InSAR) processing (Figures 2 and 3, Sentinel-1 Data Processing (SNAP)) using the SNAP (Sentinel Application Platform, version 8.0.2) from the ESA (European Space Agency, 2021) (https://step.esa.int/main/toolboxes/snap/), utilizing XML scripts for batch processing via the Graph Processing Tool (GPT).

The InSAR processing yielded thirty coherence maps at 12-day intervals. This procedure encompassed several critical steps.

- *Image preprocessing:* Reading of SLC images, Selecting VV polarization and the IW3 sub-band [12, 60] and Applying precise orbit files using third-degree polynomials (CPOD, 2022) [11].
- *Coregistration:* Aligning slave images to the master image using a cross-correlation technique [70].
- *Interferogram generation:* Calculating the complex interferogram I as [29].
- $$I = S_1 S^*_2 \qquad (1)$$
- where S_1 and S_2 are the complex SAR images and $*$ denotes complex conjugate.
- *Coherence estimation:* Computing the local coherence γ (window size: 2 pixels in azimuth, 10 pixels in distance) as [20].

$$\gamma = \frac{\left|\sum_{i=1}^{N} S_1(i) S_2^*(i)\right|}{\sqrt{\sum_{i=1}^{N} |S_1(i)|^2 \sum_{i=1}^{N} |S_2(i)|^2}} \qquad (2)$$

- where S_1 and S_2 are the complex SAR images, $*$ denotes complex conjugate and
- N is the number of pixels in the estimation window (Ferretti et al., 2007) [20].
- Correction of residual atmospheric phase par polynˆome 2D de degr´e 5 (Gomba et al., 2017) [23].
- Sub-band recombination and adaptive denoising (De Zan and Monti Guarnieri, 2006) [12].
- Geometric correction: Applying terrain correction using DEM SRTM 1 Arc-Second Global elevation data (SRTM 1Sec HGT, https://www2.jpl.nasa.gov/srtm/, Farr et al., 2007) [17, 76, 77].
- Noise filtering (Lee-Sigma 3x3) (Lee, 1983, 2009) [33–35].
- Resampling to UTM 28N WGS84 (Small and Schubert, 2008) [78].

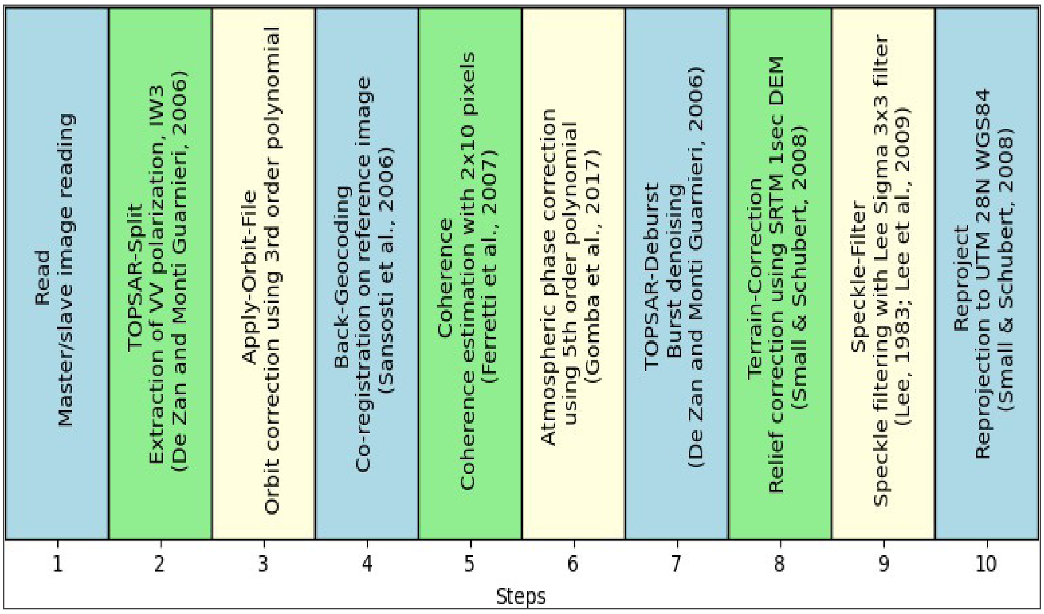

Figure 2. *Workflow for generating coherence products from Sentinel-1 SLC data in SNAP, developed by ESA using batch XML scripts.*

2.4.2 Coherence Analysis

Following InSAR processing, a comprehensive coherence analysis was conducted.

Identification of the most stable reference period by calculating the average interferometric coherence $\bar{\gamma}$.

$$\bar{\gamma} = \frac{1}{N}\sum_{i=1}^{N}\gamma_i \tag{3}$$

where N is the number of coherence images.

Derivation of a normalized coherence ratio R relative to the reference image [32].

$$R = \frac{\gamma}{\gamma_{ref}} \tag{4}$$

where γ is the coherence of the current image and γ_{ref} is the coherence of the reference image.

Thresholding to delineate potential erosion areas [72].

$$E = \begin{cases} 1 & \text{if } R < T \\ 0 & \text{otherwise} \end{cases} \tag{5}$$

where E is the erosion map and T is the threshold value.

2.4.3 K-means Clustering

To facilitate further analysis, the coherence products underwent additional preprocessing.

Normalization: Scaling the data to a range of [0, 1] using min-max normalization.

$$X_{norm} = \frac{X - X_{min}}{X_{max} - X_{min}} \tag{6}$$

Dimensionality reduction: Applying Principal Component Analysis (PCA) [22, 67] to reduce the dimensionality of the data while retaining 95.

An unsupervised k-means clustering algorithm was then applied to the coherence loss and coherence ratio images [54]. The k-means algorithm minimizes the within- cluster sum of squares.

$$J = \sum_{j=1}^{k}\sum_{i=1}^{n} ||x_i^{(j)} - c_j||^2 \tag{7}$$

where k is the number of clusters, n is the number of data points, $x^{(j)}$ is the i-th data point in cluster j, and c_j is the centroid of cluster j.

The optimal number of clusters was determined by maximizing the average silhouette coefficient s(i) [68].

$$s(i) = \frac{b(i) - a(i)}{\max\{a(i), b(i)\}} \tag{8}$$

where a(i) is the average distance between point i and all other points in the same cluster, and b(i) is the minimum average distance between point i and points in other clusters.

2.4.4 Climate Data Analysis

To complement the SAR data analysis, climate data for the study area was extracted from the NASA POWER CERES/MERRA2 database (https://power.larc.nasa.gov/ data-access-viewer/). These daily values were averaged over 12-day intervals to align with the temporal resolution of the coherence images.

The entire analytical workflow, including coherence ratio calculation [32] and k- means clustering [54], was executed using Python 3.10.9 and the scikit-learn library [61],

3. Results

This study examines the interaction between wind-driven dunes and urban areas, influenced by environmental factors. The spatiotemporal dynamics are analyzed using coherence data, wind speed, and precipitation.

Table 1 presents the key analysis parameters from February 2020 to February 2021, including average coherence, areas of low and high coherence, percentages of stability patterns, erosion areas, average coherence ratio, maximum wind speed, and average precipitation.

The period of March 15, 2020, serves as a reference for delineating stable and unstable areas (Figure 4). Areas with low coherence (< 0.3) indicate unstable dunes, while high coherence (> 0.97) represents urban infrastructures. The k-means algorithm identifies different patterns in each coherence image and calculates percentages of eroded zones relative to the reference.

Wind speeds and precipitation data provide insights into aeolian processes and their impact on sand transport and dune evolution. The coherence ratio, calculated at 1.5, allows for quantification of temporal variations in dune stability and urban area interactions over the annual cycle.

Key findings reveal seasonal variations in dune stability, with peak instability observed between June and September. A strong correlation between wind speed and erosion rates was identified, with a threshold of 9 ms identified for significant ero- sion. The study also noted a limited impact of precipitation on dune dynamics in this hyperarid region. Spatial variability in erosion patterns was particularly pronounced in northern and western dune areas and around infrastructure.

These results provide valuable insights into the spatiotemporal distribution of wind-driven sand and the evolution of dunes and urban areas, offering a quantitative basis for analyzing erosion processes in this arid coastal environment.

Table 1. *Analysis of sand dune dynamics on a beach over an annual cycle from February 8 to February 24, 2021.*

Dates	Element 1[1]	Element 2[2]		Element 3[3]			Element 4[4]			Element 5[5]	
	AC	LCS	HCS	UP	MSP	SP	Er	NEr	ARC	AWS10M	APC
8-20 Feb	0.6713	0.615473	0.055178	15	39,4	45,6	5,7	94,2	0,103	7.54	0
3-15 Mar	0.7425	0.513632	0.0769767	10,6	32,5	56,8	-	-	-	7.10	0
15-27 Mar	0.6733	0.654473	0.0447896	15,6	38,2	46,3	4	96	0,069	9.26	0.14
27 Mar -8 Apr	0.6928	0.685127	0.0747628	12,7	37,4	49,9	3,7	96,2	0,068	7.57	0
8-20 Apr	0.7293	0.653962	0.0832779	11,5	32,5	56	3,6	96,4	0,068	8.78	0
20 Apr-2 May	0.7222	0.701817	0.0798719	11,3	33	55,7	3,3	96,7	0,062	9.19	0
2-14 May	0.7040	0.637272	0.0362744	12,7	34,1	53,2	3,2	96,9	0,055	9.54	0
14-26 May	0.6921	0.718506	0.044449	13.9	35,3	50,8	4,5	95,5	0,081	8.51	0
26 May-7 Jun	0.6919	0.557059	0.0381478	12,7	35,2	52,1	2,2	97,8	0,038	8.53	0.01
7-19 Jun	0.6266	1.34982	0.0386587	19,4	38,3	42,3	12,4	87,6	0,22	10.19	0.04
19 Jun-1 Jul	0.6859	0.666223	0.0463223	16	36,3	47,7	3,5	96,5	0,06	9.79	0
1-13 Jul	0.6955	0.558252	0.0483659	14,8	35	50,3	2,6	97,3	0,046	8.20	0
13-25 Jul	0.7392	0.452323	0.0703349	10,9	31,3	57,8	1,4	98,6	0,025	7.53	0
25 Jul-18 Aug	0.6988	0.726	0.060798	15,5	35,3	49,2	3,2	96,8	0,056	8.94	0.04
18-30 Aug	0.7332	0.582094	0.0791907	11,2	32	56,8	0,8	99,2	0,014	7.18	0.01
30 Aug-11 Sep	0.6340	0.611897	0.0446193	17,6	39,8	42,6	7,9	92,1	0,135	7.10	0.03
11-23 Sep	0.6897	0.701646	0.0851512	12,7	36,2	51,1	3,6	96,4	0,064	6.40	0.15
23 Sep-5 Oct	0.6761	0.668097	0.042235	15	37,3	47,7	3,7	96,2	0,065	8.69	0.01
5-17 Oct	0.7412	0.539689	0.0963912	10,6	31,6	57,8	0,7	99,3	0,012	6.53	7.60
17-29 Oct	0.7153	0.459476	0.0684616	12,2	34,7	53,1	0,5	99,5	0,008	7.53	0.04
29 Oct-10 Nov	0.7203	0.413665	0.0604574	12	35	52,9	1,4	98,7	0,024	7.07	0
10-22 Nov	0.6772	0.597251	0.082767	14,9	38,3	46,9	2,7	97,2	0,046	6.57	0
22 Nov-4 Dec	0.6723	0.449769	0.062501	14,3	38,4	47,3	4,3	95,7	0,074	6.25	0
4-16 Dec	0.7247	0.471738	0.0739113	11,3	33,6	55	2,5	97,6	0,044	7.70	0
16-20 Dec	0.7123	0.595718	0.0676101	11,5	34,2	54,3	3,3	96,8	0,058	7.32	0
28 Dec-9 Jan	0.7287	0.386757	0.0573919	10,7	33,7	55,6	1,5	98,5	0,028	6.06	0
9-21 Jan	0.6142	0.821369	0.0337199	19,4	39,4	41,1	10,7	89,3	0,184	9.60	0
21 Jan-2 Feb	0.6629	0.560466	0.0514314	15,8	39,5	44,7	5,5	94,5	0,097	8.03	0
2-14 Feb	0.6989	0.621264	0.0735707	13,6	36,4	50	3	96,9	0,055	7.45	0.01
14-26 Feb	0.6651	0.691428	0.0596059	15,3	38,2	46,5	6	94	0,106	8.17	0

The columns represent different analysis parameters at regular intervals (12 days) over the period from February 2020 to February 2021, including.

[1] *The average coherence of surfaces (AC for Avg Coherence).*

[2] *The low coherence surface area (LCS for Low Coherence Surface (km^2)), The high coherence surface area (HCS for High Coherence Surface (km^2)).*

[3] *The percentage of unstable patterns (large dunes) (UP for Unstable Pattern (%)), The percentage of medium stable patterns (small dunes) (MSP for Medium Stable Pattern (%)), The percentage of stable patterns (impervious and urban areas) (SP for Stable Pattern (%)).*

[4] *The non-erosion rate (NEr, (%)), The average ratio of coherence (ARC for Avg Ratio of Coherence).*

[5] *The average maximum wind speed over 12 days at 10 meters altitude (Wind Speed max at 10 meters), The average corrected precipitation over 12 days (APC for Avg PRECTOTCORR, mm/12 days).*

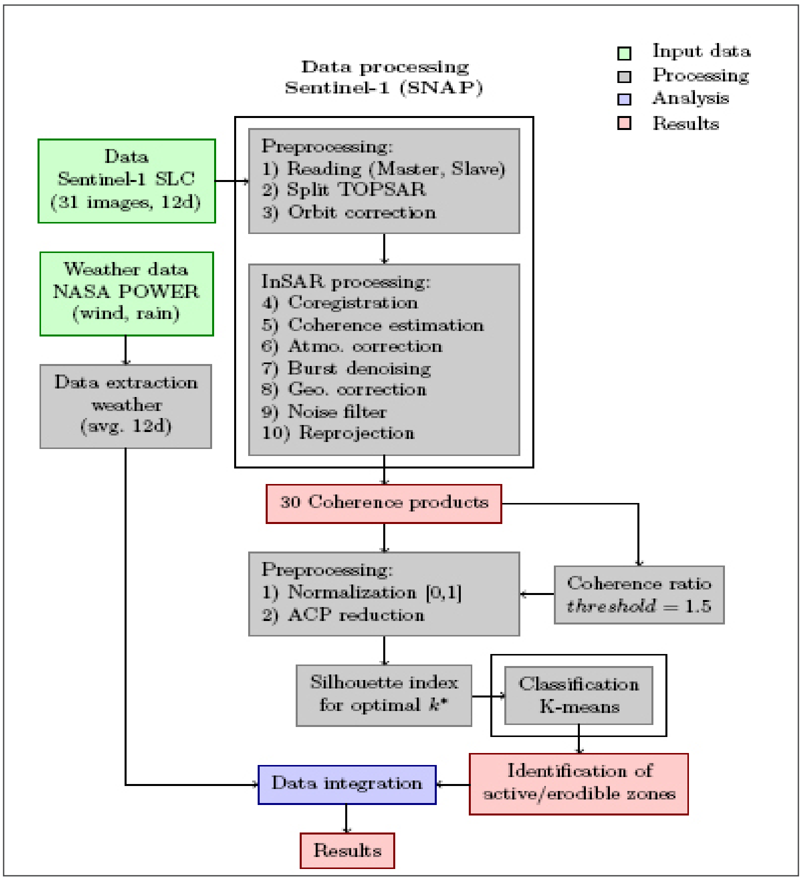

Figure 3 . *Detailed methodological workflow illustrating the various steps involved in this project. Different phases are represented by distinct colored rectangles: green for input data, gray for processing steps, blue for analyses, and red for final results.*

3.1 InSAR-Coherence

3.1.1 Variations in Mean Coherence

Figure 4 illustrates mean coherence trends in the Boulenouar study area from February 2020 to February 2021. Mean coherence ranges from 0.6142 to 0.7425, indicating seasonal variations in surface stability. Higher coherence is observed in spring, while lower values occur in winter due to weather conditions (Figure 13 and Table 1). Significant increases in coherence (April, July, and October 2020) demonstrate more pronounced stability of aeolian sand patterns.

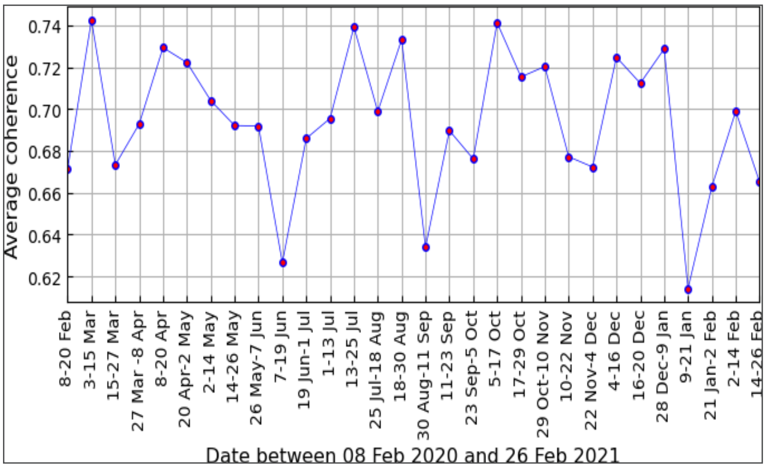

Figure 4 . *Mean coherence of a 30-image dataset.*

3.1.2 Reference Period and Zone Delimitation

The coherence image from March 3-15, 2020 (Figure 5) serves as a reference, clearly distinguishing between active and inactive surfaces. Dune and vegetation areas appear in black (low coherence), while urban areas are displayed in light tones (high coherence). Spatial analysis reveals coherence values ranging from 0.18 to 0.994, with significant changes near transportation routes and large sand dunes.

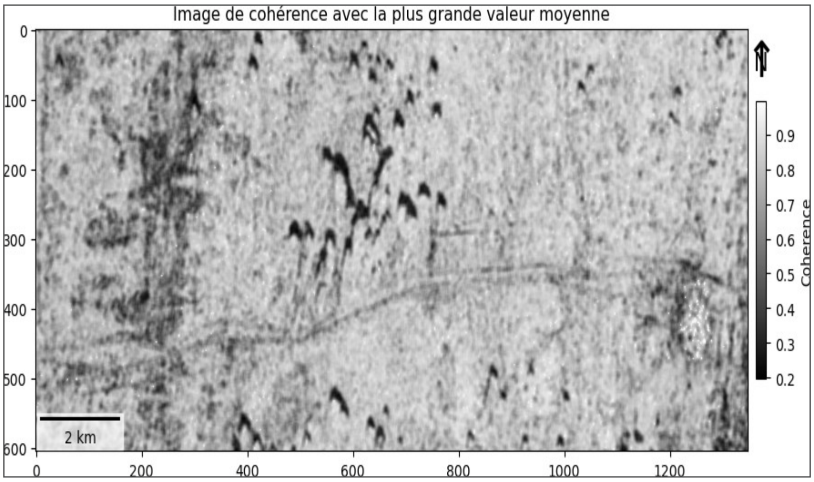

Figure 5. *Reference coherence image (March 3-15, 2020). Light tones indicate stable areas (Urban Zone), darker tones indicate unstable areas (Sand Dune Field).*

Figure 6 confirms higher stability in urban areas (coherence up to 0.994) compared to dune fields (up to 0.65). This contrast highlights the utility of InSAR coherence for monitoring changes between urban and dune landscapes.

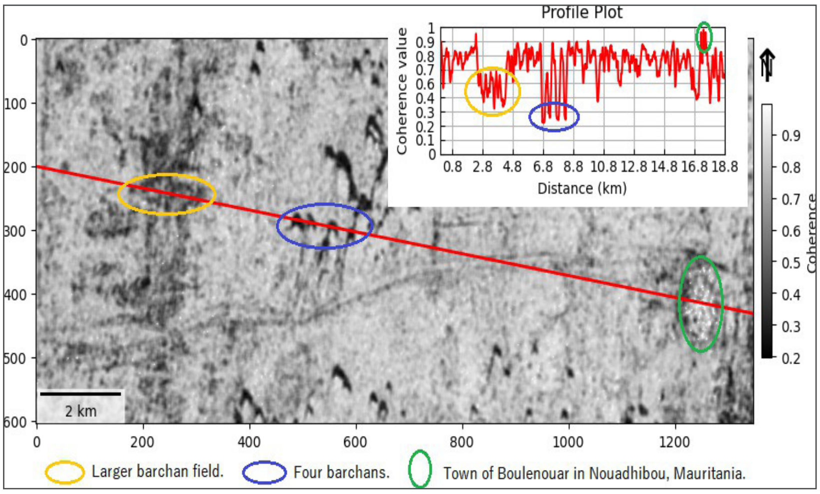

Figure 6. *Coherence image with section analysis. The red curve represents coherence values along the illustrated section.*

3.1.3 Direction of Dune Movement

Comparison of coherence images from the beginning and end of the study period (Figure 7) reveals sand dune movement towards the south and southwest. This analysis is based on extracted coherence values below 0.6 using Python 3.10.

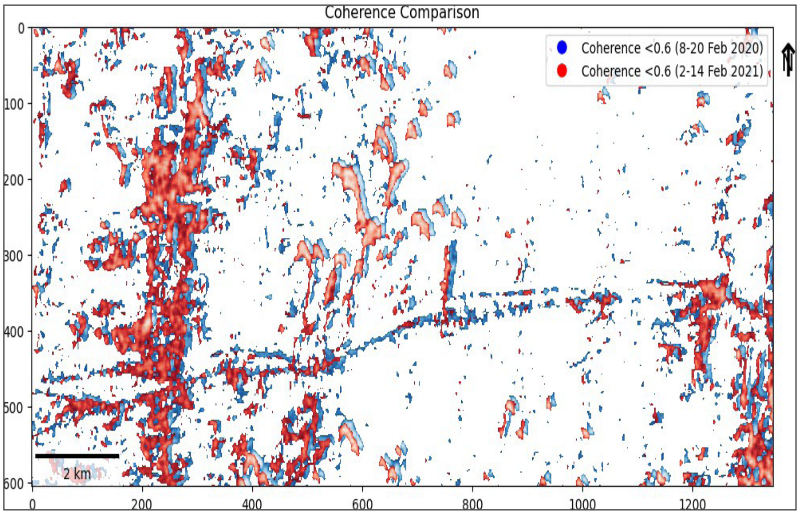

Figure 7. *Spatio-temporal evolution of sand dunes based on Sentinel-1 SLC IW coherence data. Blue: 2020 dunes, Red: 2021 dunes (coherence < 0.6).*

These results demonstrate the effectiveness of InSAR-Coherence technique in dis- tinguishing areas of human activity from natural areas, particularly for large sand dunes and urban zones. The method provides valuable insights into the relationships between InSAR-Coherence, topography, and wind speed, contributing to a better understanding of aeolian processes in the region.

3.1.4 Surface Area Estimations

Coherence thresholds were used to quantify surface areas of dunes (< 0.3) and urban zones (> 0.97). Figures 8 and 9 illustrate seasonal variations in these areas.

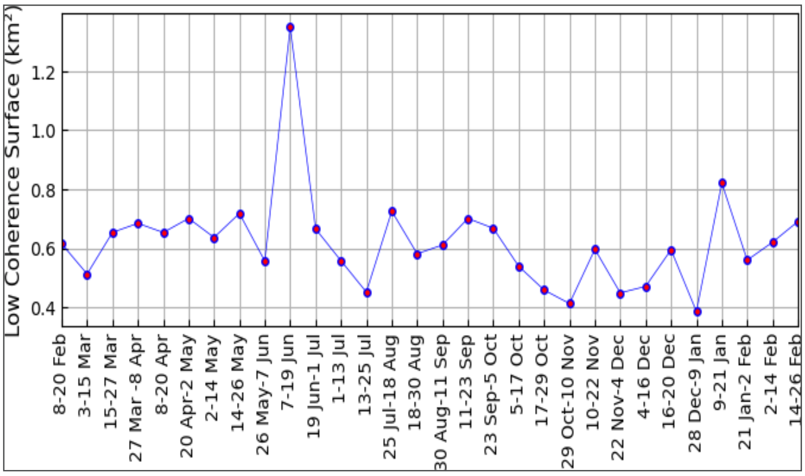

Figure 8. *Low coherence surface area (in km , < 0.3) from a dataset of 30 images.*

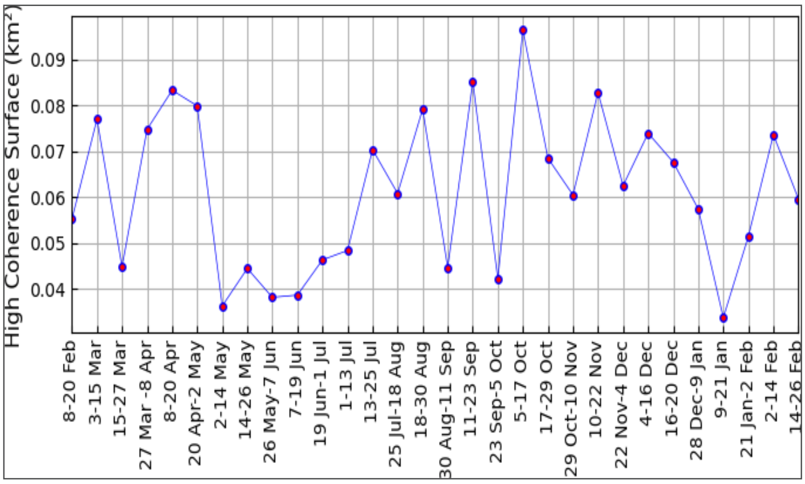

Figure 9. *High coherence surface area (in km , > 0.97) from a dataset of 30 images.*

Low coherence surfaces, indicative of increased mobility, were maximal between June 7-19, 2021 (1.349 km). High coherence surfaces, reflecting greater stability, showed their maximum extent between May 2-14, 2021 (0.036 km). Over a 13-month period (February 2020 to February 2021), dunes expanded by 0.075785 km , while urban areas increased by 0.0042579 km (Table 2).

Table 2. *Evolution of surface area (in km) of different zones (Large dunes/Urban) between February 8-20, 2020 and February 14-26, 2021*

	Element 1[1]			**Element 2[2]**		
Zones	Area1	Area2	Area diff	Precision (km^2)	Area diff	Vr
Large dunes	0.615473	0.691428	0.075955	0.00017	0.075785	0.075785
Urban	0.055178	0.0596059	0.0044279	0.00017	0.0042579	0.0042579

Area1=Surface area February 8-20, 2020 (km), Area2=Surface area February 14-26, 2021 (km), Area diff=Area difference (km), Vr=Rate of variation in 1 year (km /year).

[1] *Example for a first table footnote.*

[2] *Example for a second table footnote.*

These observations suggest that dunes, primarily fed by north-to-south winds, pose a potential threat to infrastructure. Urban areas appear to expand southward along transportation routes.

3.2 K-Means Classification

3.2.1 Determining an Appropriate Number of Clusters using the Silhouette Score

Figure 10 presents silhouette scores for coherence image datasets and coherence ratios. For coherence images, the optimal score of 0.202 is achieved with k = 3 clusters. For coherence ratios, although the score is maximized for k = 5 clusters (0.186), we opted for k = 2 clusters (score 0.178) for physical interpretability and classification simplicity.

This approach allows for efficient discrimination between eroding and stable zones, facilitating analysis of dune dynamics and urban expansion in the study area.

3.2.2 Monitoring Spatio-Temporal Patterns with K-Means Results

Analysis of coherence patterns related to aeolian sand mobility from February 8, 2020 to February 26, 2021 (Figure 11, Table 1) reveals the annual cycle of dune dynamics in the Boulenouar region. Unstable patterns, indicating greater dune mobility, peaked between June and September, reaching 19.4% of the surface area in June 7-19. Stable patterns were most extensive in spring, covering 56 − 57% between April 8-20 and May 2-14. Large mobile dunes consistently exceeded 12% during summer, compared to <13% in other seasons. Significant variability was observed, with the proportion of mobile dunes varying by a factor of 1.8 between June 2020 (19.4%) and July 2020 (10.9%).

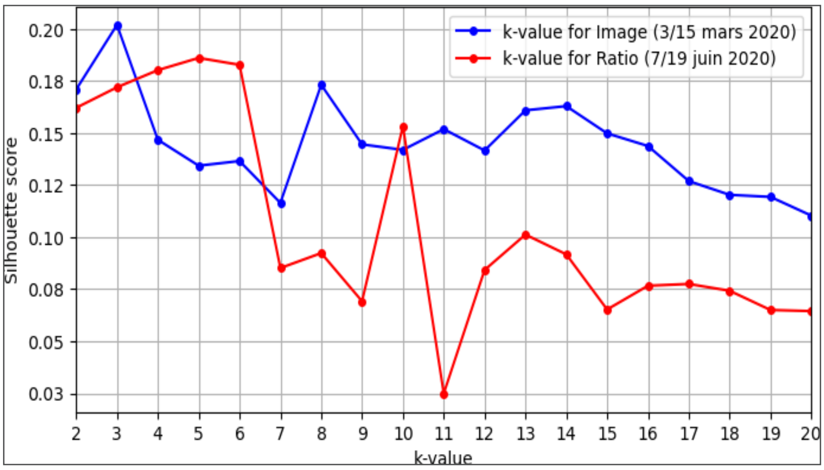

Figure 10. *Silhouette scores as a function of k (ranging from 2 to 20) for coherence images (Blue) and coherence ratios (Red).*

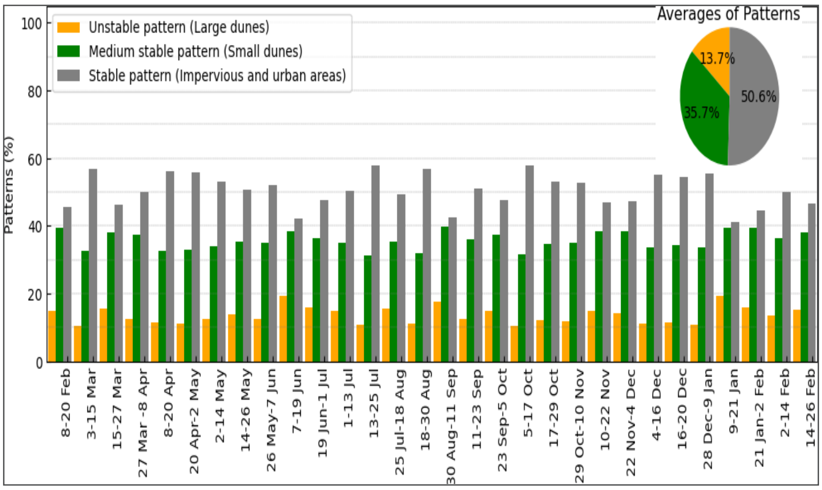

Figure 11. *Inventories of three patterns from different parts of the study area between 2020 and 2021. Each pattern is represented by a different color in the graph: Unstable pattern (Big dunes, Yellow), medium stable pattern (Small dunes, Green), and stable pattern (Impervious and urban areas, Gray). The annual average proportion of each pattern is shown in the top right corner.*

These seasonal contrasts reflect the influence of meteorological conditions, particu- larly wind speed. Spring-summer 2020 wind speeds (10-12 m/s) were 1.5 times higher than winter-spring 2020 (6-8 m/s), explaining increased dune mobility.

Overall, the data indicate relative stability of the dune field, with the stable pattern predominant (~50% of observations) throughout the year. This suggests well-established dune morphology with mature, perennial crests. The average radar coherence of ~0.7 (Figure

4) confirms the prevalence of slowly evolving sandy surfaces.

A correlation between pattern stability and dune size was observed: large dunes were most dynamic (unstable pattern) while small dunes and flat areas evolved slowly (stable pattern). The medium pattern represented an intermediate situation. Relative percentages of each pattern varied with meteorological conditions, particularly wind speed.

Annually, approximately 13.69% of dune massifs remained subject to aeolian changes, with the remainder displaying a stable pattern (Figure 11).

3.2.3 Coherence Ratio and Erosion Percentage

Coherence ratio images compared changes relative to the March 2020 reference image (March 3-15) using a mean threshold of 1.5. This method, correlated with erosion percentages (Figures 12 and 13), enabled quantitative and qualitative evaluation of spatio-temporal variations in aeolian dynamics. Key findings from the coherence ratio analysis include an average erosion of 3.84% over the studied period. The mean ratio varied from 0.008 (October 17-29, 2020) to 0.22 (June 7-19, 2020). Low mean ratios (<0.06) coincided with little erosion (0.8-5%), suggesting stability, while high ratios (>0.1) corresponded to significant erosion rates (7.9-13.1%), indicating substantial sediment movement.

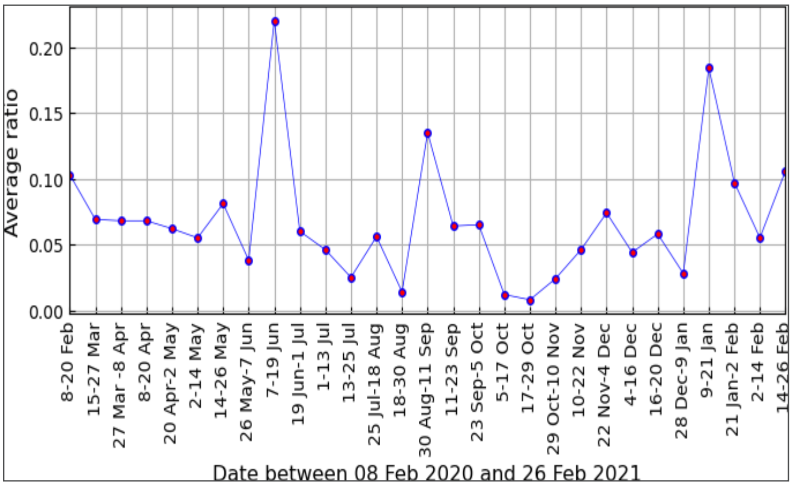

Figure 12. *Mean coherence ratio for each date relative to March 3/15, 2020.*

3.2.4 Reference Image Ratio

The coherence ratio image (Figure 14) facilitated precise identification of erosion areas. Values above 1.5 indicated coherence loss compared to the reference image, suggesting aeolian processes such as erosion and deposition. Most affected areas included dune regions in the north and west, northeastern parts of Nouadhibou, railway routes, and areas around Boulenouar.

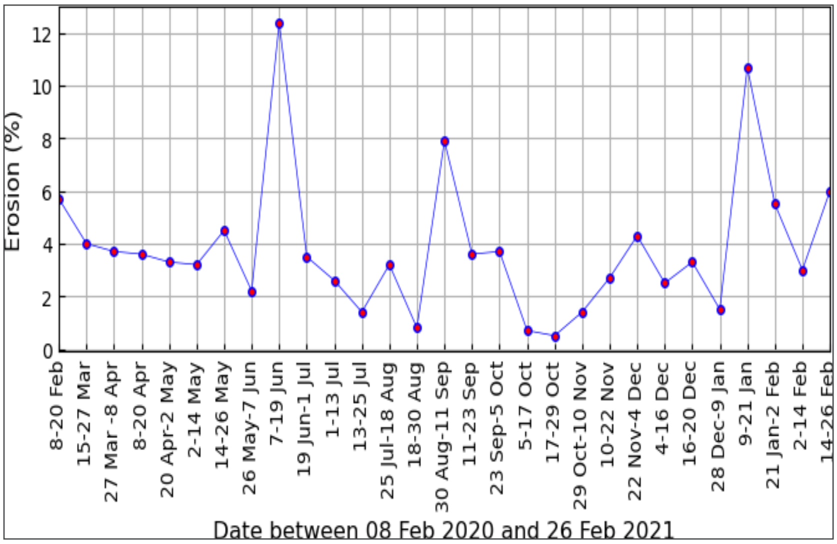

Figure 13. *Percentage of coherence loss for each date relative to March 3/15, 2020.*

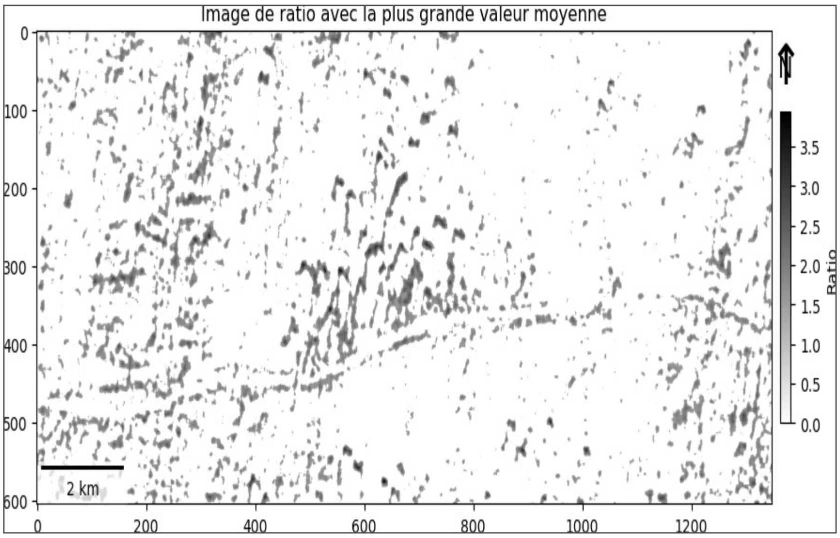

Figure 14. *Coherence ratio image (June 7-19, 2020 relative to March 3-15, 2020) highlighting changes in sandy areas.*

3.2.5 Meteorological Conditions

Figure 15 illustrates the correlated evolution of precipitation, wind speed, and esti- mated erosion rate from February 8, 2020, to February 26, 2021. A systematic correlation between wind intensity and erosion levels was observed, with wind speeds >9 m/s significantly promoting erosion. The highest erosion (12.4%) occurred June 7-19, 2020, with 10.19 m/s wind gusts. Precipitation generally had negligible impact, except during rare extreme events.

This analysis clearly demonstrates the cause-effect relationship between wind inten- sity and erosion, highlighting the predominant role of wind conditions in coastal dynamics.

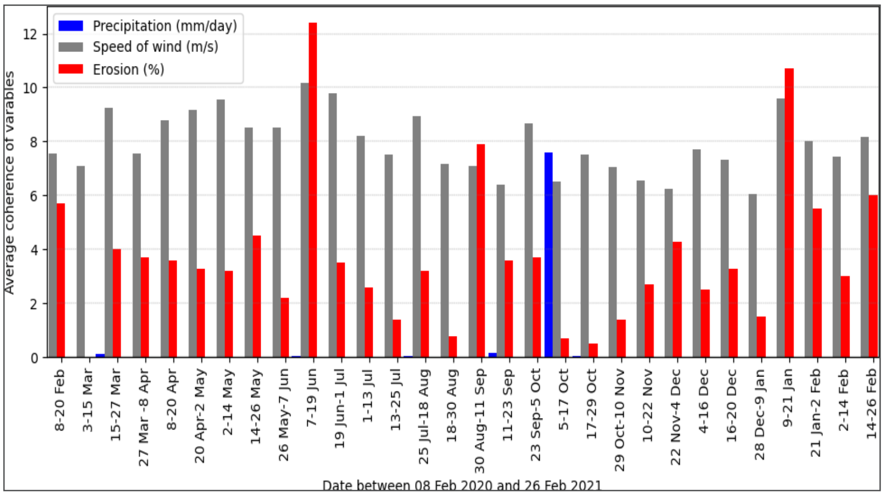

Figure 15. *Temporal evolution of average precipitation (mm/day, Blue), maximum wind speed (m/s, Gray), and erosion rate (%, Red) from February 8, 2020, to February 26, 2021.*

3.2.6 Seasonal Interpretation

Analysis of the data presented in Table 1 reveals a marked seasonal dynamic in the evolution of sand dunes on the studied beach. This dynamic is primarily influenced by wind conditions, as well as the nature of surfaces, represented by average coherence (AC) and erosion (Er). Precipitation (APC) seems to have a negligible impact on dune dynamics.

At the beginning of the year, from February to April, a progressive increase in the average coherence of surfaces (AC) is observed, indicating dune stabilization, while erosion (Er) remains relatively high. This coincides with moderate winds (AWS10M) between February 8 and April 20. This period corresponds to late winter and early spring, when wind conditions are generally calmer, favoring dune consolidation.

During the summer months, from June 7 to September 11, the average coherence of surfaces (AC) decreases, reflecting greater dune instability. This trend is accom- panied by an increase in winds (AWS10M) and high erosion (Er) during this period. The intense summer wind conditions disrupt the dune structure, leading to their displacement and reworking.

In autumn, from September 11 to December 4, the average coherence of surfaces (AC) increases again, indicating dune restabilization, while erosion (Er) gradually decreases. Although a precipitation peak is observed from October 5 to 17, its impact seems limited compared to wind conditions. The calmer autumn wind conditions generally allow for a progressive reconsolidation of dunes.

Finally, during winter, from December 28 to February 26, the average coherence of surfaces (AC) is lower, indicating greater dune instability. This is likely due to winter conditions with stronger winds (AWS10M), promoting erosion (Er) and dune rework- ing. This period represents a transition phase before the return of spring conditions more conducive to dune stabilization.

4. Discussion

The results of this study demonstrate the utility of the interferometric coherence technique for accurate and repeated monitoring of sand dune dynamics subject to aeolian processes in desert environments.

Analysis of the dense time series of Sentinel-1 coherence images allowed for the identification of areas exhibiting high aeolian activity throughout the year (19.4% of dunes classified as highly active by k-means classification). These areas logically correspond to barchan and transverse dune types known for their high mobility under the action of prevailing northeast winds in this region (Hachemi et al., 2013 [28]).

Figure 4 well illustrates the seasonal variation of detected aeolian activity, with higher levels of sand accumulation and erosion in spring and summer, in phase with stronger winds and rare rain events favoring deflation. These results align with observations from previous studies on desert dune dynamics (Tsoar and Pye, 1987 [81]; Kok et al., 2012 [47]).

The coherence ratio approach developed by Lee and Liu (2001) has also proven effective in precisely mapping areas undergoing significant erosion/sedimentation between two given dates. As shown in Figure 14, an annual erosion of 3.84% was quantified, mainly located in the north and west of the study area as well as along road and rail transport axes.

This worrying progression of mobile barchan dune fields towards vital socio- economic infrastructure aligns with concerns raised by previous works (Bodart and Ozer, 2007 [8]; Hugenholtz et al., 2012 [38]; Hachemi et al., 2013 [28]; Abdelkareem et al., 2020 [2]). It underscores the urgency of sustainable management of natural resources in this region highly vulnerable to natural hazards.

From a methodological standpoint, our results reinforce the interest in exploiting the rich archive of Sentinel-1 radar images with high spatial (5x20m) and temporal (12 days) resolution for this type of environmental monitoring applications (ESA, 2018, 2019). The coupling of InSAR signal processing algorithms with unsupervised classification techniques such as k-means has proven particularly effective, paving the way for future developments in machine learning (Li and Chen, 2007 [49]; Liu et al., 2019 [52]; Lu¨a et al., 2021 [36]).

Some limitations of this preliminary study deserve mention. First, the absence of field data to quantitatively validate the results obtained by remote sensing is a con- straint. It would be interesting in the future to acquire in-situ measurements (DGPS, drone photogrammetry) on sites of particular interest such as identified high-erosion areas.

Next, the use of higher spatial resolution radar images (< 5m), for example from future Terrasar-X NG or NISAR missions, would allow for refined morphological anal- yses at the scale of individual dunes. The contribution of Sentinel-2 optical data at 10m spatial resolution could also prove beneficial in multi-sensor fusion mode.

Finally, the development of artificial intelligence algorithms dedicated to the auto- matic extraction of geomorphological characteristics of dune fields (type, orientation, dynamics) would constitute a major advance for effective operational management of natural risks in these fragile desert territories.

5. Conclusion

This study, utilizing Sentinel-1 radar data, has enabled precise monitoring and map- ping of sand dune dynamics and aeolian erosion/sedimentation processes in the desert region of Boulenouar, Mauritania. The approach combining differential radar inter- ferometry, coherence ratio monitoring, and unsupervised k-means classification has proven effective in identifying and quantifying areas of intense aeolian activity and morphological changes in dune fields. A marked seasonal cycle has been evidenced, with maximum erosion/sedimentation levels in spring and summer, correlated with dominant strong winds. Approximately 19.4% of the dune surface was classified as extremely active in 2020-2021, and a concerning annual erosion of 3.84% was iden- tified in areas located to the north, west, and along vital terrestrial transport axes, threatening these essential economic infrastructures.

In the future, the integration of data from other high-resolution optical satellite sensors, the use of precise digital terrain models derived from stereoscopic acquisitions or airborne lidar, as well as coupling with numerical simulations of aeolian dynam- ics would allow for a more comprehensive multi-sensor characterization of aeolian processes. This would open interesting perspectives for better understanding the 3D migration of dunes and predicting their future evolution.

These results underscore the importance of continuing remote sensing monitoring and considering sustainable land management strategies to preserve road and rail networks and urban areas from progressive sand encroachment.

6. References

1. Abba, M., Essahlaoui, A., Elkharki, O., & Mechbouh, J. (2019). The Use of Interferometric Coherence of Sentinel-1a Images to Study Silting in South- East Morocco. Annals of Ecology and Environmental Science, 3, 37–49 https://doi.org/10.22259/2637-5338.0302005.
2. Abdelkareem, M., Gaber, A., Abdalla, F., & El-Din, G.K. (2020). Use of optical and radar remote sensing satellites for identifying and monitoring active/ inac- tive landforms in the driest desert in Saudi Arabia. Geomorphology, 362, 107197 https://doi.org/10.1016/j.geomorph.2020.107197.
3. Ali, S. Z., & Dey, S. (2019). Bed particle saltation in turbulent wall-shear flow: A review. Proceedings of the Royal Society A: Mathematical, Physical and Engi- neering Sciences, 475(2228), 20190025 https://doi.org/10.1098/rspa.2019.0025.
4. Angelov, P., and X. Gu. 2019. Empirical Approach to Machine Learn- ing, IEEE Transactions on Cybernetics. Springer International Publishing. https://doi.org/10.1109/TCYB.2017.2753880.
5. Arthur, D., & Vassilvitskii, S. (2007). K-means++: The Advan- tages of Careful Seeding. SODA ’07: Proceedings of the Eighteenth Annual ACM-SIAM Symposium on Discrete Algorithms, 1027–1035https://theory.stanford.edu/ sergei/papers/kMeansPP-soda.pdf.
6. Bagnold, R. A. (1941). The physics of blown sand and desert dunes. London: Methuen.
7. Bamler, R., & Hartl, P. (1998). Synthetic aperture radar interferometry. Inverse Problems, 14(4), R1-R54 https://doi.org/10.1088/0266-5611/14/4/001.
8. Bodart, C., & Ozer, A. (2007). The Use of Sar Interferometric Coherence Images to Study Sandy Desertification in Southeast Niger: Preliminary Results. European Space Agency, (Special Publication) ESA SP: Noordwijk, The Netherlands.
9. Braun, A. (2021). Retrieval of digital elevation models from Sentinel-1 radar data – open applications, techniques, and limitations. Open Geosciences, 13, 532–569 https://doi.org/10.1515/geo-2020-0246.
10. Celik, T. (2009). Unsupervised Change Detection in Satellite Images Using Prin- cipal Component Analysis and k-Means Clustering. IEEE Geoscience and Remote Sensing Letters, 6, 1457.
11. Copernicus Sentinel POD Service File Format Specification. (2022). ESA. COPERNICUS PRECISE ORBIT DETERMINATION SERVICE (CPOD).Retrieved March 7, 2021, from https://sentinel.esa.intdocuments247904/351187Copernicus Sentinels POD Service File Format Specification.
12. De Zan, F., & Monti Guarnieri, A. (2006). TOPSAR: Terrain Observation by Progressive Scans. IEEE Transactions on Geoscience and Remote Sensing, 44, 2352–2360 https://doi.org/10.1109/TGRS.2006.873853.
13. Dempster, A. P., Laird, N. M., & Rubin, D. B. (1977). Maximum Likelihood from Incomplete Data Via the EM Algorithm. Journal of the Royal Statistical Society: Series B (Methodological). https://doi.org/10.1111/j.2517-6161.1977.tb01600.x.
14. Dhanachandra, N., Manglem, K., & Chanu, Y.J. (2015). Image Segmentation Using K-means Clustering Algorithm and Subtrac- tive Clustering Algorithm. Procedia Computer Science, 54, 764–771. https://doi.org/10.1016/j.procs.2015.06.090.
15. Duan, W., Zhang, H., Wang, C., & Tang, Y. (2020). Multi-Temporal InSAR Par- allel Processing for Sentinel-1 Large-Scale Surface Deformation Mapping. Remote Sensing, 12, 3749. https://doi.org/10.3390/rs12223749.
16. European Space Agency, 2016 Sentinel-1 Toolbox: TOPS Interferometry Tutorial.
17. Farr, T. G., Rosen, P. A., Caro, E., Crippen, R., Duren, R., Hensley, S., Kobrick, M., et al. (2007). The Shuttle Radar Topography Mission. Reviews

of Geophysics, 45(2), RG2004. https://doi.org/10.1029/2005RG000183.

18. Fattahi, H., Agram, P., & Simons, M. (2017). A Network-Based Enhanced Spectral Diversity Approach for TOPS Time-Series Analy- sis. IEEE Transactions on Geoscience and Remote Sensing, 55, 777–786. https://doi.org/10.1109/TGRS.2016.2614925.
19. Ferretti, A., Prati, C., & Rocca, F. (2001). Permanent Scatterers in SAR Interferometry. IEEE Transactions on Geoscience and Remote Sensing, 39(1), 8-20.
20. Ferretti, A., Monti-Guarnieri, A., Prati, C., Rocca, F., & Massonnet, D. (2007). InSAR Principles: Guidelines for SAR Interferometry Processing and Interpretation. TM-19, ESA Publications: Noordwijk, The Netherlands.
21. Gaber, A., Abdelkareem, M., Abdelsadek, I., Koch, M., & El-Baz, F. (2018). Using InSAR Coherence for Investigating the Interplay of Fluvial and Aeolian Features in Arid Lands: Implications for Groundwater Potential in Egypt. Remote Sensing, 10, 832. https://doi.org/10.3390/rs10060832.
22. Gimeno, M., and J. San-Miguel-Ayanz. 2004. “Evaluation of RADARSAT-1 Data for Identification of Burnt Areas in Southern Europe.” Remote Sensing of Environment 92 (3): 370–375.
23. Gomba, G., Gonz´alez, F. R., & De Zan, F. (2017). Ionospheric phase screen compensation for the Sentinel-1 TOPS and ALOS-2 ScanSAR modes. IEEE Transactions on Geoscience and Remote Sensing, 55(1), 223-235. https://doi.org/10.1109/TGRS.2016.2604461.
24. Hachemi, K., Jurchescu, M., Grecu, F., Ozer, A., & Visan M.C. (2014). Study of Some Lakes in the North-Eastern Romanian Plain Using the Coherence Image of the Tandem Pair (ERS-1 and ERS-2). Advances in Remote Sensing, 3(1), 23-32.
25. Hachemi K. (2009). Apport de l’interf´erom´etrie radar SAR pour la r´ealisation d’un MNA (Mod`ele Num´erique d’Altitude) sur la r´egion subcarpatique de Buzˇau (Roumanie). Journal Analele Universitatii Bucuresti, Annee LVIII – 2009, 5-38.
26. Hachemi, K., Abdellaoui, A., Ozer, A., Grecu, F., & Visan M. C. (2012). Utilit´e de l’image de coh´erence du couple tandem (ers-1/2) dans la d´elimitation et le calcul des dimensions des lacs et de la v´eg´etation dans la zone de Buzˇau en Roumanie. Revue T´el´ed´etection, 11(3), 389-400.
27. Hachemi, K., Amrouni, Y., Daoudi, M., & Bamousa, A.O. (2020). Diachronic study of the great Sebkha of Oran (western Algeria) based on SAR radar images (1992–2011). Journal of Taibah University for Science, 14, 1433–1446.
28. Hachemi K, & Thomas YF (2013). Analyse de la mobilit´e d’un champ de Barkhanes (Mauritanie) `a partir des images SAR. In: Conf´erence internationale de G´eomatique et d’Analyse Spatiale SAGEO (Spatial Analysis and GEOmatics), IUEM, Brest, France, 23–26.
29. Hanssen RF. (2001). Radar interferometry: data interpretation and error analysis. Dordrecht, Netherlands: Kluwer Academic Publishers.
30. Havivi, S., Amir, D., Schvartzman, I., August, Y., Maman, S., Rotman, S.R., & Blumberg, D.G. (2018). Mapping dune dynamics by InSAR coherence. Earth Surface Processes and Landforms, 43, 1229–1240.
31. Ho Tong Minh, D., Hanssen, R., & Rocca, F. (2020). Radar Interferometry: 20 Years of Development in Time Series Techniques and Future Perspectives. Remote Sensing, 12, 1364.
32. Lee, H., & Liu, J. G. (2001). Analysis of topographic decorrelation in SAR inter- ferometry using ratio coherence imagery. IEEE Transactions on Geoscience and Remote Sensing, 39, 223–232.
33. Lee, J. S. (1983). Digital image smoothing and the sigma filter. Computer Vision, Graphics, and Image Processing, 24(2), 255–269.
34. Lee, J. S. (1983). A simple speckle smoothing algorithm for synthetic aperture radar images. IEEE Transactions on Systems, Man, and Cybernetics, SMC-13(1), 85–89.
35. Lee, J. S., Wen, J. H., Ainsworth, T. L., Chen, K. S., & Chen, A. J. (2009). Improved Sigma Filter for Speckle Filtering of SAR Imagery. IEEE Transactions on Geoscience and Remote Sensing, 47(1), 202–213.
36. Lu¨a, P., Narteau, C., Dong, Z., Rozier, O., & Courrech du Pont, S. (2021). Direct validation of dune instability theory. Proceedings of the National Academy of Sciences, 118(17), e2024105118.
37. Hooper, A., Segall, P., & Zebker, H. (2007). Persistent scatterer interferometric synthetic aperture radar for crustal deformation analysis, with application to Volc´an Alcedo, Gal´apagos. Journal of Geophysical Research (Solid Earth), 112, B07407.
38. Hugenholtz, C.H., Levin, N., Barchyn, T.E., & Baddock, M.C. (2012). Remote sensing and spatial analysis of aeolian sand dunes: A review and outlook. Earth- Science Reviews, 111, 319–334.
39. Jain, A. (2010). Data Clustering: 50 Years beyond K-means. Pattern Recognition Letters, 31(8), 651–666.

40. Jiang, H., Huang, N., & Zhu, Y. (2014). Analysis of Wind-blown Sand Movement over Transverse Dunes. Scientific Reports, 4, 7114.

41. Lee, J.-S., & Jurkevich, I. (2009). Improved Sigma Filter for Speckle Filtering. IEEE Transactions on Geoscience and Remote Sensing, 47(1), 202-213.

42. Hachemi, K., Thomas, Y.-F., & Martin, T. (2020). Classification of dune dynamics from SAR images :case study of the barchans of north-east of Nouadhibou, Mauritania (1995-2010). PHOTO INTERPRE´TATION EUROPEAN JOURNAL OF APPLIED REMOTE SENSING 2019/1-2-3-4, 55, 43.

43. Kim, J.-R., Dorjsuren, M., Choi, Y., & Purevjav, G. (2020). Reconstructed Aeo- lian Surface Erosion in Southern Mongolia by Multi-Temporal InSAR Phase Coherence Analyses. Frontiers in Earth Science, 8.

44. Kim, J.-R., Lin, C.-W., & Lin, S.-Y. (2021). The Use of InSAR Phase Coherence Analyses for the Monitoring of Aeolian Erosion. Remote Sensing, 13.

45. Kirschner, G.K., Xiao, T.T., & Blilou, I. (2021). Rooting in the Desert: A Developmental Overview on Desert Plants. Genes, 12, 709.

46. Kodinariya, T. M., & Makwana, P. R. (2013). Review on Determining Number of Cluster in K-Means Clustering. International Journal of Advance Research in Computer Science and Management Studies, 1, 2321–7782.

47. Kok, J. F., Parteli, E. J., Michaels, T. I., & Karam, D. B. (2012). The physics of wind-blown sand and dust. Reports on Progress in Physics, 75(10), 106901.

48. Lacko´ov´a, L., Lieskovsky´, J., Nikseresht, F., Halabuk, A., Hilbert, H., Hal´aszov´a, K., & Bahreini, F. (2023). Unlocking the Potential of Remote Sensing in Wind Erosion Studies: A Review and Outlook for Future Directions. Remote Sensing, 15, 3316.

49. Li, J., & Chen, W. (2007). Clustering synthetic aperture radar (SAR) imagery using an automatic approach. Canadian Journal of Remote Sensing, 33, 303–311.

50. Li, M., Zang, S., Zhang, B., Li, S., & Wu, C. (2014). A Review of Remote Sens- ing Image Classification Techniques: The Role of Spatio-contextual Information. European Journal of Remote Sensing, 47(1), 389–411.

51. Li, Y., & Wu, H. (2012). A Clustering Method Based on K-Means Algorithm. Physics Procedia, 25, 1104–1109.

52. Liu, L., Jia, Z., Yang, J., & Kasabov, N.K. (2019). SAR Image Change Detec- tion Based on Mathematical Morphology and the K-Means Clustering Algorithm. IEEE Access, 7, 43970–43978.

53. Liu, L.-L., Wen, X.-B., & Gao, X.-X. (2010). Segmentation for SAR Image Based on a New Spectral Clustering Algorithm. In: Li, K., Jia, L., Sun, X., Fei, M., Irwin, G.W. (Eds.), Life System Modeling and Intelligent Computing, Lecture Notes in Computer Science. Springer, Berlin, Heidelberg, pp. 635–643. https://doi.org/10.1007/978-3-642-15615-1 75.

54. MacQueen, J. (1967). Some Methods for Classification and Analysis of Multivari- ate Observations. Proceedings of the Fifth Berkeley Symposium on Mathematical Statistics and Probability.

55. Madsen, S.N., Zebker, H.A., & Martin, J. (1993). Topographic mapping using radar interferometry: processing techniques. IEEE Transactions on Geoscience and Remote Sensing, 31, 246–56.

56. Manzoni, M.; Molinari, M.E.; Monti-Guarnieri, A. Multitemporal InSAR Coher- ence Analysis and Methods for Sand Mitigation. Remote Sens. 2021, 13, 1362.

57. Massonnet, D., & Rabaute, T. (1993). Radar interferometry: limits and potential. IEEE Transactions on Geoscience and Remote Sensing, 31, 455–64.

58. Monti Guarnieri, A., & Tebaldini, S. (2007). Hybrid Cram´er⍰Rao bounds for crustal displacement field estimators in SAR interferometry. IEEE Signal Processing Letters, 14, 1012–1015.

59. Nagpal, A., Jatain, A., & Gaur, D. (2013). Review Based on Data Clustering Algo- rithms. 2013 IEEE Conference on Information and Communication Technologies, 298–303.

60. Nestor Yague-Martinez, Pau Prats-Iraola, Senior Member, IEEE, Fernando Rodriguez Gonzalez, Ramon Brcic, Member, IEEE, Robert Shau, Senior Member, IEEE, Dirk Geudtner, Michael Eineder, Senior Member, IEEE, and Richard Bam- ler, Fellow, IEEE (2016). Interferometric Processing of Sentinel-1 TOPS Data. IEEE TRANSACTIONS ON GEOSCIENCE AND REMOTE SENSING, VOL. 54, NO. 4.

61. Pedregosa, F., Varoquaux, G., Gramfort, A., Michel, V., Thirion, B., Grisel, O., Blondel, M., et al. (2011). Scikit-learn: Machine Learning in Python. Journal of Machine Learning Research, 12, 2825–2830.

62. Phiri, D., & Morgenroth, J. (2017). Developments in Landsat Land Cover Classification Methods: A Review. Remote Sensing, 9, 967.

63. Programme des Nations Unies pour le D´eveloppement (PNUD). (2014). Plan d'Action National pour l'Environnement et le D´eveloppement Durable (PANEDD) de la Mauritanie. UNDP.

64. Pye, K., & Tsoar, H. (2009). Aeolian Sand and Sand Dunes. Springer Berlin Heidelberg, Berlin, Heidelberg. https://doi.org/10.1007/978-3-540-85910-9.

65. Quegan, S., Le Toan, T., Yu, J. J., Ribbes, F., & Floury, N. (2000). Multitemporal ERS SAR Analysis Applied to Forest Mapping. IEEE Transactions on Geoscience and Remote Sensing, 38(2), 741–753.

66. Rehman, T. U., Mahmud, M. S., Chang, Y. K., Jin, J., & Shin, J. (2019). Current and Future Applications of Statistical Machine Learning Algorithms for Agricul- tural Machine Vision Systems. Computers and Electronics in Agriculture, 156, 585–605.

67. Richards, J. A. 2013. Remote Sensing Digital Image Analysis: An Introduction.5th ed. Berlin Heidelberg.: Springer.

68. Rousseeuw, P. J. 1987. Silhouettes: A Graphical Aid to the Interpretation and Val- idation of Cluster Analysis. Journal of Computational and Applied Mathematics 20: 53–65. https://doi.org/10.1016/0377-0427(87)90125-7.

69. Rosen, P.A., Hensley, S., Joughin, I.R., Li, F.K., Madsen, S.N., Rodr´ıguez, E., & Goldstein, R.M. (2000). Synthetic Aperture Radar Interferometry. PROCEED- INGS OF THE IEEE, 88.

70. Sansosti, E., Berardino, P., Manunta, M., Serafino, F., & Fornaro, G. (2006). Geo- metrical SAR image registration. IEEE Transactions on Geoscience and Remote Sensing, 44, 2861–2870 https://doi.org/10.1109/TGRS.2006.875787.

71. Santoso, A. W., Pebrianti, D., Bayuaji, L., & Zain, J. M. (2015). Perfor- mance of Various Speckle Reduction Filters on Synthetic Aperture Radar Image. 2015 4th International Conference on Software Engineering and Com- puter Systems, ICSECS 2015: Virtuous Software Solutions for Big Data, 11–14 https://doi.org/10.1109/ICSECS.2015.7333103.

72. Schepanski, K., Wright, T.J., & Knippertz, P. (2012). Evidence for flash floods over deserts from loss of coherence in InSAR imagery. Journal of Geophysical Research: Atmospheres, 117, D20101 https://doi.org/10.1029/2012JD017580.

73. Schmidt, H., and A. Karnieli (2000), Remote sensing of the seasonal vari- ability of vegetation in a semi-arid environment, J. Arid Environ., 45, 43–59. https://doi.org/10.1006/jare.1999.0607.

74. Senthilnath, J., Kandukuri, M., Dokania, A., & Ramesh, K. N. (2017). Application of UAV Imaging Platform for Vegetation Analysis Based on Spectral-spatial Methods. Computers and Electronics in Agriculture, 140, 8–24 https://doi.org/10.1016/j.compag.2017.05.027.

75. Shao, Y. (2009). Physics and Modelling of Wind Erosion. Atmospheric and Oceanographic Sciences Library, Vol. 3. Springer https://doi.org/10.1007/978-1-4020-8895-7.

76. Small, D. (1998). Generation of digital elevation models through spaceborne SAR interferometry. Doctoral dissertation/PhD. Zu¨rich: University of Zu¨rich.

77. Small, D. (2011). Flattening Gamma: Radiometric Terrain Correction for SAR Imagery. IEEE Transactions on Geoscience and Remote Sensing, 49(8), 3081–3093 https://doi.org/10.1109/TGRS.2011.2120616.

78. Small, D., & Schubert, A. (2008). Guide to ASAR Geocoding. Report RSL-ASAR- GC-AD. Remote Sensing Laboratories, University of Zurich, Zurich, Switzerland.

79. Soni, K. G., & Patel, D. A. (2017). Comparative Analysis of Kmeans and K-medoids Algorithm on Iris Data. International Journal of Computational Intelligence Research, 5, 33–37 https://doi.org/10.5120/888-1261.

80. Subasi, A. 2020. “Chapter 2 - Data Prepocessing.” In Practical Machine Learning for Data Analysis Using Python, 27–89. Accademic Press. https://doi.org/10.1016/B978-0-12-821379-7.00002-3.

81. Tsoar, H., & Pye, K. (1987). Dust transport and the question of desert loess formation. Sedimentology, 34, 139–153 https://doi.org/10.1111/j.1365- 3091.1987.tb00566.x.

82. World Bank. (2021). Climate change knowledge portal: Mauritania https://climateknowledgeportal.worldbank.org/country/mauritania/climate- data-historical.

83. Yao, Z. Y., Wang, T., Han, Z. W., Zhang, W. M., & Zhao, A. G. (2007). Migration of sand dunes on the northern Alxa Plateau, Inner Mongolia, China. Journal of Arid Environments, 70(1), 80-93 https://doi.org/10.1016/j.jaridenv.2006.12.012.

84. Xing, T., Hu, Q., Li, J., & Wang, G. (2016). Refined SAR image segmentation algorithm based on K-means clustering. CIE International Conference on Radar (RADAR), 1–3 https://doi.org/10.1109/RADAR.2016.8059487.

85. Zebker, H. A., & Villasenor, J. (1992). Decorrelation in interfero- metric radar echoes. Geophysical Research Letters, 19(2), 159-162 https://doi.org/10.1029/91GL03308.

86. Zhang, H., Wu, Z., & Hu, J. (2021). Numerical simulation of wind field and sand flux in crescentic sand dunes. Scientific Reports, 11, 12010 https://doi.org/10.1038/s41598-021-84509-x.